Accuracy evaluation and mechanism crossover of single-electron transfer in Si tunable-barrier turnstiles

Gento Yamahata,* Katsuhiko Nishiguchi, and Akira Fujiwara
NTT Basic Research Laboratories, NTT Corporation, 3-1 Morinosato Wakamiya, Atsugi, Kanagawa 243-0198, Japan
(Received 8 May 2013; revised manuscript received 20 March 2014; published 8 April 2014)

Using an error-counting scheme, we evaluated the accuracy of single-electron (SE) transfer in Si tunable-barrier turnstiles in a dilution refrigerator. The error counting was performed by shuttling SEs between a lead and a charge-accumulating node and detecting in real time the number of electrons in the node with an SE-resolution charge sensor. The best experimentally obtained error rate is about 100 parts per million (ppm), where the SE capture in the SE island occurs in thermal equilibrium due to the heating effect on SEs caused by pulse voltages applied to modulate the potential barrier. When we reduce the heating effect by suppressing the pulse voltages, there is a change in the SE transfer mechanism to nonequilibrium SE capture. We theoretically discuss the crossover point of the change. Moreover, at the minimum pulse voltage, the theoretical lower bound of the error rate estimated by fitting is on the order of 0.01 ppm. This suggests that Si SE-transfer devices are promising candidates for use as quantum current standards in metrology.

DOI: 10.1103/PhysRevB.89.165302 PACS number(s): 73.23.Hk, 85.35.Gv, 73.40.Qv

I. INTRODUCTION

Single-electron (SE) transfer has been attracting much interest for applications to SE circuits [1], on-demand SE sources [2], and quantum current standards in metrology, which could allow us to redefine the ampere by fixing the elementary charge e [3]. Quantum current standards can also be used for quantum metrology triangle experiments, which provide a consistency check for the existing two electric standards: the quantum Hall resistance standard and the Josephson voltage standard [4]. For these applications, it is necessary to realize an SE transfer error rate of better than 0.01 parts per million (ppm) and a current level larger than several hundred picoamperes [5].

In pioneering work [6,7], the SE transfer was demonstrated by using arrays of metallic islands separated by oxide tunnel barriers. Periodic gate modulation at a frequency f generates a quantized current $I = nef$, where the n electrons in a group are transferred one by one. By increasing the number of tunnel barriers, an error rate of 0.015 ppm has been achieved [8]. Although this value almost satisfies the accuracy criterion, the current level ($\sim$ a few picoamperes), which is limited by the fixed and large tunneling time constant, is not high enough for the current standards. In another approach using hybrid superconducting-normal metal turnstiles [9], a quantized current has been clearly generated but the criteria for the current standards have not yet been satisfied. On the other hand, semiconductor-based SE transfer driven by electrostatically induced tunable barriers [10–13] allows us to generate a high (nanoampere level) current with gigahertz operation [13]. Thus, the accuracy of semiconductor-based devices should be investigated toward current standards.

Two main approaches have been used to evaluate the accuracy of SE transfer: a comparison of current generated by the SE transfer with that generated by primary standards [14] and error counting with an SE-resolution sensor during SE shuttle transfer, which is called shuttle error measurement [15]. With the former method, an error rate of about 1.2 ppm has been reported in a GaAs-based SE pump, which represents the best data obtained to date for semiconductor-based SE transfer [16], although a magnetic field of 14 T is necessary to improve the accuracy [17]. However, the primary standards determine the upper bound of the measurable accuracy of the SE transfer. In contrast, the latter method has no such upper bound, thus allowing us to explore the true accuracy of the SE transfer. Using the latter method, we have evaluated the accuracy of the SE transfer in Si metal-oxide-semiconductor field-effect transistors (MOSFETs) and shown that the error is due to thermal fluctuations at 17 K, where the error rate was still high ($\sim 2 \times 10^4$ ppm) [18].

In this paper, we report single-shot shuttle error measurements in Si MOSFETs at a base temperature of 30 mK and in a zero magnetic field. The best obtained error rate is about 100 ppm. Furthermore, we reveal the mechanism that dominates the error rate and indicate the potential for further reduction of the error rate to about 0.04 ppm.

II. DEVICE STRUCTURE AND MEASUREMENT SCHEMES

Figure 1(a) shows a scanning electron microscope (SEM) image of the device. The left and right parts of the device are a charge sensor and an SE transfer device, respectively. The device fabrication process is as follows. First, Si nanowires and a side gate (SSG) on a 400-nm-thick buried oxide layer were formed by using electron beam lithography, followed by thermal oxidation for the formation of a 40-nm-thick gate oxide layer. The nanowires should be 20 nm thick and 10 and 30 nm wide, respectively, for the charge sensor and the SE transfer device. Next, three polycrystalline-Si lower gates (LG1, LG2, LG3) with a gate length of 30 nm were formed on the nanowire for the SE transfer device. The gap between LG1 and LG2 was 130 nm. Then, a 50-nm-thick interlayer oxide was grown by chemical vapor deposition. After that, the entire region seen in the SEM image was covered with a polycrystalline-Si gate, which is referred to as an upper gate.

*yamahata.gento@lab.ntt.co.jp

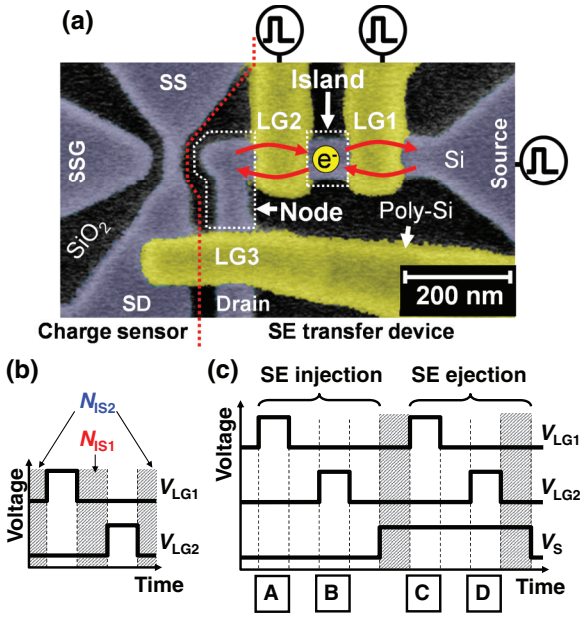

FIG. 1. (Color online) (a) Scanning electron microscope image of the device before upper gate formation. The wide upper gate covers the whole region shown in the image. The charge sensor and the SE transfer device are on the left and right sides of the dotted line, respectively. (b) Pulse sequence of the SE turnstile operation. The pulse voltages are applied to LG1 (V_{LG1}) and LG2 (V_{LG2}). N_{IS1} and N_{IS2} are the numbers of electrons in the island at the regions indicated by arrows. (c) Pulse sequence of the SE shuttle transfer. In addition to V_{LG1} and V_{LG2}, the pulse voltages are applied to the source (V_S).

Finally, n-type leads (source and drain for the SE transfer device; SS and SD for the charge sensor) were formed by ion implantation with the upper gate used as a mask.

The SE transfer is performed by using a turnstile operation with high-frequency pulse voltages alternately applied to LG1 and LG2 [Fig. 1(b)], where a small charge island is formed between LG1 and LG2, yielding quantized current plateaus $I = nef$ [11]. For the SE shuttle transfer, we apply one more pulse voltage to the source to change the direction of the SE transfer. In addition, a charge-accumulating node is electrostatically created between LG2 and LG3. As a result, an SE is transferred from the source to the node (SE injection), then returns from the node to the source (SE ejection). The pulse sequence for the SE shuttle transfer is shown in Fig. 1(c). The charge sensor, which has sufficient sensitivity for SE detection [19], counts the number of electrons in the node (N_{node}) during the SE shuttle transfer to determine the number of errors. Since the error rate of SE injection is significantly different from that of SE ejection as discussed below, we used single-shot error detection to evaluate the injection and ejection errors separately; the time intervals of the two hatched regions in Fig. 1(c), which have the same voltage conditions, are four orders of magnitude longer than the other time intervals. In addition, the time interval of the right hatched region is about double that of the left one. The rise time of the pulse voltage is 2 ns. All the measurements were performed in a dilution refrigerator at a base temperature of 30 mK and in a zero magnetic field.

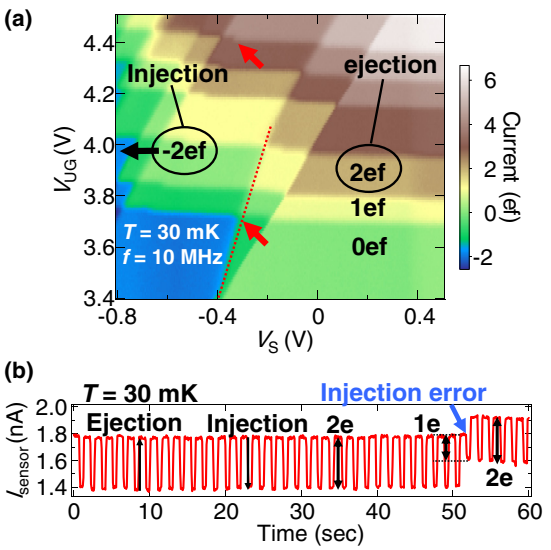

FIG. 2. (Color online) (a) Two-dimensional plot of the current passing through the SE transfer device as a function of V_S and voltages applied to the upper gate (V_{UG}), where the current is normalized by ef. Voltages applied to the drain (V_D) and LG3 (V_{LG3}) are -0.9 and 1.5 V, respectively. V_{LG1} and V_{LG2} are modulated between -3 and 0.5 V. The dotted line and red arrows indicate irregular characteristics. (b) Sensor current I_{sensor} as a function of time during the 2-SE shuttle transfer ($V_{LG3} = -3$ V, $V_{UG} = 4.14$ V, $V_D = -0.9$ V). The voltages applied to SD (V_{SD}), SS (V_{SS}), and SSG (V_{SSG}) are 1 mV, 0 mV, and -3.1 V, respectively. V_{LG1} and V_{LG2} are modulated between -3 and 0.5 V. V_S is modulated between -0.72 and 0.7 V. The voltage conditions do not correspond to $\pm 2ef$ plateaus in (a) presumably because of the different V_{LG3} and the feedback effect discussed in Sec. III C. The pulse rise time is 2 ns.

III. RESULTS AND DISCUSSION

A. SE turnstile operation and 2-SE shuttle transfer

Figure 2(a) shows the current, which is normalized by ef, observed during SE turnstile operation as a function of voltages applied to the source (V_S) and the upper gate (V_{UG}). The clear current plateaus nef ($-nef$) indicate the SE transfer from drain to source (from source to drain). Additionally, Fig. 2(a) helps us to explore the voltage conditions for the SE shuttle transfer. We decided to use $2ef$ and $-2ef$ plateaus in the SE shuttle transfer (2-SE shuttle transfer) because they are relatively clear and wide. They correspond to the ejection and injection of 2 SEs and hereafter we call them 2-SE ejection and 2-SE injection, respectively. In the current diagram, we can see certain irregularities indicated by red arrows that are probably due to the SE transfer via trap levels [18]. However, we confirmed experimentally that most of the current plateaus including $2ef$ originate from the SE transfer via a charge island [20]. The error rate of the island-mediated SE transfer is determined by the electron addition energy, E_{add}, which is estimated from the width of the current plateau [21].

We detected changes of N_{node} in real time during the 2-SE shuttle transfer, as shown in Fig. 2(b). The abrupt increase and decrease in the current correspond to 2-SE ejection and injection, respectively. It is beneficial that this measurement does not suffer from measurement noise because the charge

sensor has sufficient sensitivity. At the point indicated by the blue arrow, the current amplitude is half, which means that just one electron is injected in error. We count such errors to estimate the error rate of the SE shuttle transfer.

B. Details of the 2-SE shuttle transfer: Effect of the charging in the node

To understand the results of the shuttle error measurements shown later, we first consider the 2-SE shuttle transfer procedure in detail. Figure 3(a) is a stability diagram of the SE turnstiles [11]. We define the number of electrons captured in the island immediately after the fall of the pulse applied to LG1 and LG2 as N_{IS1} and N_{IS2}, respectively [see also Fig. 1(b)]. Since the island is coupled to the upper gate and the source during the LG1 modulation (there is a large potential barrier under LG2), the boundary for N_{IS1} is given by $V_{UG} = V_S + eN_{IS1}/C_{UG} + \text{const.}$ [red lines in Fig. 3(a)], where C_{UG} is the capacitance between the upper gate and the island. By contrast, during the LG2 modulation, the island is coupled to the upper gate and node (there is a large potential barrier under LG1), giving the boundary for N_{IS2} as $V_{UG} = eN_{IS2}/C_{UG} + \text{const.}$ [blue lines in Fig. 3(a)]. The total number n of electrons transferred from the node to the source is given by $n = N_{IS2} - N_{IS1}$, resulting in the current plateaus nef. Note that the distances between each boundary are determined by E_{add}.

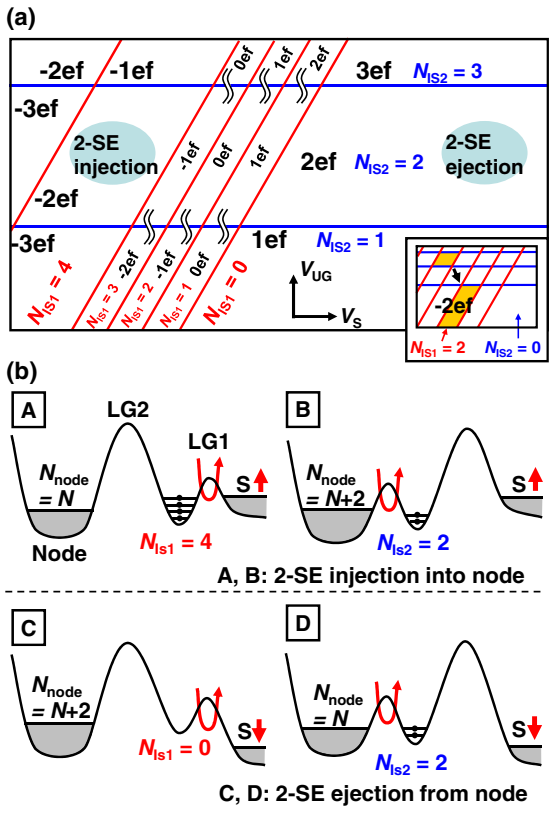

FIG. 3. (Color online) (a) Stability diagram of the SE turnstile as a function of V_{UG} and V_S. $nef (n = -3, -2, \ldots, 3)$ is the current plateau. The operating points for the 2-SE shuttle transfer are located in the $\pm 2ef$ plateaus. N_{IS1} and N_{IS2} are the numbers of electrons captured in the island just after the fall of the pulse applied to LG1 and LG2, respectively. The red and blue lines are the boundaries for N_{IS1} and N_{IS2}, respectively. (Inset) The movement of the position of the 2-SE injection ($-2ef$ plateau) toward the region where $N_{IS1} = 2$ and $N_{IS2} = 0$. (b) Potential diagrams corresponding to operating points A, B, C, and D in Fig. 1(c), where the number of electrons in the node (N_{node}) is assumed to be N or $N + 2$.

The two gates, LG1 and LG2, are each modulated two times per cycle for the 2-SE shuttle transfer, as indicated by operating points A, B, C, and D in Fig. 1(c). A potential diagram corresponding to the four points is shown in Fig. 3(b). First, at operating point A, where we assume $N_{node} = N$, LG1 is modulated and $N_{IS1} = 4$. Next, LG2 is modulated at operating point B, where $N_{node} = N + 2$ because $N_{IS2} = 2$. These two processes correspond to the 2-SE injection into the node and the operating points are located in the $-2ef$ plateau in Fig. 3(a). To perform the 2-SE ejection from the node, the operating point is moved to the $2ef$ plateau, which is indicated in Fig. 3(a), by changing V_S. Then, LG1 is modulated at operating point C, where $N_{IS1} = 0$ and $N_{node} = N + 2$. After that, LG2 is modulated at operating point D, where $N_{IS2} = 2$ and $N_{node} = N$. Finally, to perform the 2-SE injection again, the operating point is moved to the $-2ef$ plateau by changing V_S. The 2-SE shuttle transfer is performed by repeating these procedures.

In the 2-SE shuttle transfer, when the electron addition energy in the node, E_{add}^{node}, is not much smaller than E_{add}, the potential change in the node caused by SE charging is not negligible. As a result, the SE capture probability in the island at operating point B ($N_{node} = N + 2$) is different from that at operating point D ($N_{node} = N$). In addition, when 2-SE injection or ejection errors occur, both N_{node} and the error rate change. Thus, E_{add}^{node} should be minimized if we are to investigate the error rate properly. Note that charging the node has no effect on the SE capture probability in the island at operating points A and C because the node is decoupled from the island.

Although we can increase the node size to reduce E_{add}^{node}, this would reduce the SE resolution of the sensor. Thus, we need an optimized design for the device structure. Alternatively, the effect of node charging can be reduced by moving the operating points for the 2-SE injection to the region where $N_{IS1} = 2$ and $N_{IS2} = 0$ [inset in Fig. 3(a)]. Since the position of operating point B can be set sufficiently far from the blue lines, the errors at operating point B can be neglected.

C. Error rate estimated by shuttle error measurements

To estimate the tiny error rate of the 2-SE shuttle transfer, we performed a longer measurement as shown in Fig. 4(a), in which the horizontal axis is compressed compared with that in Fig. 2(b). Although the sensor current should change between two levels without errors, the observed sensor current fluctuated between more than two levels due to transfer errors. A notable feature is that most of the errors occurred during the 2-SE injection. This could be related to the trap levels that disturb the stability diagram shown in Fig. 2(a). The fact that the irregular lines in the stability diagram in Fig. 2(a) correspond to the red lines in Fig. 3(a) indicates that the trap levels could be located under LG1 and N_{IS1} may be

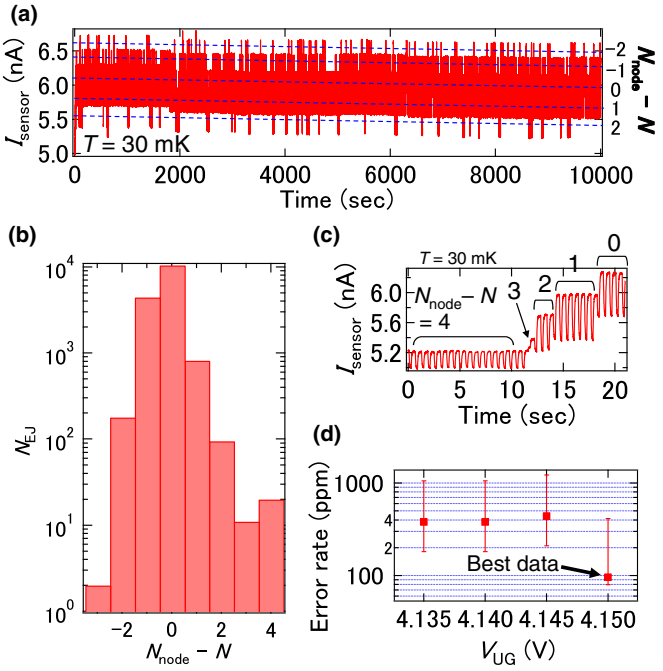

FIG. 4. (Color online) (a) Sensor current I_{sensor} as a function of time taken by the long-term 2-SE shuttle transfer ($V_{LG3} = -3$ V, $V_{UG} = 4.15$ V, $V_{SD} = 5$ mV, $V_{SS} = 0$ mV, $V_{SSG} = -3.75$ V, $V_D = -0.9$ V). V_{LG1} and V_{LG2} are modulated between -3 and 0.5 V. V_S is modulated between -0.72 and 1.4 V. The rise time of the pulse is 2 ns. The frequency of the applied pulse voltage is about 1.6 Hz. The SE ejection and injection are performed in 0.2 ms. (b) Histograms of the number of 2-SE ejections (N_{EJ}) as a function of $N_{node} - N$, where N_{node} is assumed to be N at maximum N_{EJ}. (c) A magnified plot of (a), where $N_{node} - N$ is denoted. (d) The error rate of the 2-SE ejection at $N_{node} = N$ as a function of V_{UG}. V_{SSG} is different at each point: from left to right, $V_{SSG} = -3.61, -3.65, -3.70$, and -3.75 V. The error bars are calculated by using a confidence interval for the Poisson distribution.

disturbed. The mechanism of the errors induced by the trap levels deserves further experimental and theoretical study.

Next, we focus on the 2-SE ejection, in which the error at operating point C can be neglected because the ejection can be performed at a position far from the red lines in Fig. 3(a). To investigate the effect of the potential in the node, we counted the number of 2-SE ejections (N_{EJ}) when the node contained $N_{node} = N \pm i$ ($i = -3, -2, \ldots, 4$) electrons at operating point D, where N_{node} is assumed to be N at maximum N_{EJ} [Fig. 4(b)]. Note that this distribution is mainly dominated by the errors that occur during the 2-SE injection because there are many injection errors. N_{node} is also shown in Fig. 4(a) by dashed lines. The spikelike changes in the sensor current at $N_{node} = N \pm 2$ in Fig. 4(a) indicate that N_{node} tends to return to $N \pm 1$. In addition, the 2-SE ejection at $N_{node} = N + 4$ occurred only after the start of the 2-SE shuttle transfer [Fig. 4(c)] (probably due to incomplete initialization). These facts suggest that with increasing (decreasing) N_{node}, the potential in the node increases (decreases) and thereby the errors in relation to increasing (decreasing) N_{IS2} increase, resulting in a tendency for N_{node} to decrease (increase). This feedback (similar feedback has been observed with a GaAs pump [23]) indicates that the ejection errors at the operating points with maximum N_{EJ} ($N_{node} = N$) should have low error rates, which corresponds to the operating points being located near the center of the $2ef$ plateau. In addition, since the quantum current standard does not have such a node, we should disregard the effect of the charging in the node. Thus, we estimated the ejection error at $N_{node} = N$, which is defined as the number of ejection errors divided by N_{EJ}, and the best value is around 100 ppm [Fig. 4(d)]. The error rate is about 200 times better than that of the previously reported turnstile with a similar Si island [18]. Since the observed error rates correspond to those at operating point D and the rise time of the pulse voltage is fast ($t_{rise} \sim 2$ ns), this result indicates that current with an error rate of about 100 ppm can be generated at $f \sim 100$ MHz.

Note that when we changed V_{UG} and estimated the 2-SE ejection errors in the same way as shown in Fig. 4(d), the error rates were almost constant despite the different V_{UG}. This is because we have to tune the voltages applied to SSG to set the condition of the sensor to the most sensitive point for SE detection. This inevitably changes the node potential and thereby cancels out the effect of V_{UG}.

D. Theoretical model of SE transfer: Crossover of two mechanisms

We consider theoretical models to investigate the error mechanism and theoretically estimate the lower bound of the error rate. The mechanism of the SE transfer is based on a simple SE box model in thermal equilibrium [18,24] and/or the nonequilibrium decay cascade model [13,25]. In the former model [see Fig. 5(a)], the average number of electrons captured in the island is determined by the grand canonical distribution with the electrostatic energy E_n in the island, which is given by

$$\langle n \rangle = \Sigma n \exp(-E_n/kT)/\Sigma \exp(-E_n/kT), \quad (1)$$

$$E_n = (-ne + C_{UG}V_{UG})^2/2C_\Sigma + \text{const.}, \quad (2)$$

where k is the Boltzmann constant, T is the temperature, n is the number of electrons in the island, C_Σ is the total capacitance of the island, and the Fermi level in the lead $E_F \equiv 0$ [24]. With this model the plateaus of the SE transfer current have a symmetric rise shape. In the latter model [see Fig. 5(b)], the escape dynamics of the SEs from the island to the lead during the rise of the potential barrier determines the number of electrons captured in the island. First, many electrons stay in the island when the potential barrier induced by LG1 or LG2 is low. Then, as the potential barrier rises, some electrons return to the lead because the potential of the island also rises simultaneously due to capacitive coupling C_C between the lower gates and the island. The escape rate of the nth SE is much lower than that of the $(n+1)$th SE because the electrochemical potential of the nth SE is lower than that of the $(n+1)$th SE due to E_{add} and therefore the potential barrier height and width for the nth SE are both larger than those for the $(n+1)$th SE. Thus, n SEs can be captured in the island in a particular V_{UG} range, yielding the nef plateau. By solving the master equation, the formula of the decay cascade model

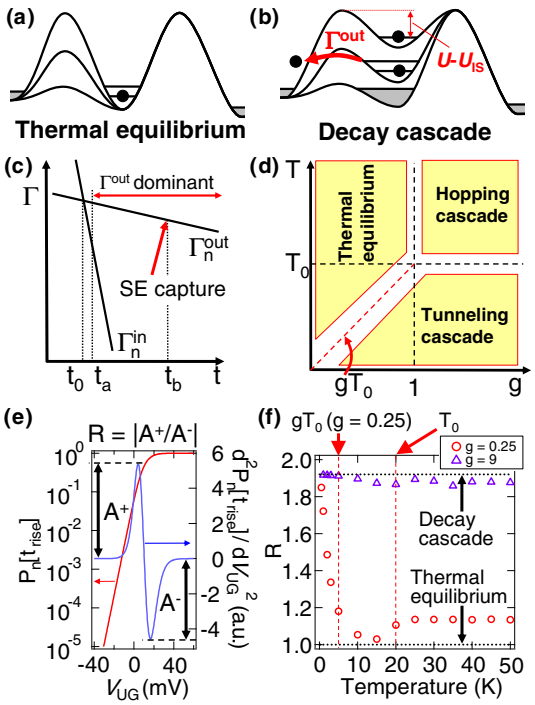

FIG. 5. (Color online) (a) Energy diagram for the thermal equilibrium model. (b) Energy diagram for the decay cascade model. (c) Schematic diagram of the rate at which the nth SE enters the island ($\Gamma_n^{\rm in}$) and escapes from it ($\Gamma_n^{\rm out}$) as a function of time. In this case, the decay cascade model is valid. (d) Diagram for the crossover of the transfer mechanism as a function of g (defined in the main text) and temperature (T). (e) Calculated probability P_n of capturing the nth SE in the island at $t = t_{\rm rise}$ and second derivative of P_n as a function of $V_{\rm UG}$. R is defined as the ratio of the two peak heights A^+ and A^-. (f) Calculated R as a function of temperature, where g is 0.25 and 9. The parameters used in the calculation are given in Appendix A. The two horizontal dotted lines indicate $R = 1$ (thermal equilibrium model) and $R = 1.92$ (decay cascade model). The two vertical dotted lines indicate $T_0 = 20$ K and $gT_0 = 5$ K ($g = 0.25$).

is given as

$$\langle n\rangle = n - 1 + \Sigma_{k=n}^{n+1}\exp[-\exp(-\alpha_{\rm UG}V_{\rm UG} + \Delta_k)], \qquad (3)$$

where $\alpha_{\rm UG}$ and Δ_k are fitting parameters [13,25]. Note that we assume that the escape rates of the nth and $(n+1)$th SEs ($\Gamma_n^{\rm out}$ and $\Gamma_{n+1}^{\rm out}$, respectively) have the same time dependence. The parameters Δ_n and Δ_{n+1} are related to $\Gamma_n^{\rm out}$ and $\Gamma_{n+1}^{\rm out}$ as $\Delta_{n+1} - \Delta_n = \ln(\Gamma_{n+1}^{\rm out}/\Gamma_n^{\rm out}) \equiv \delta_{n+1}$, which corresponds to the width of the nth plateau as a function of $V_{\rm UG}$. This indicates that the error rate of the SE transfer, which is determined by the width of the plateau, should be low when the difference between the escape rates of the nth and $(n+1)$th SEs is large. In addition, this model yields an asymmetric rise shape of the plateaus of the SE transfer current.

To clarify the crossover point of the two models, we consider how the nth SE is captured in the island using the master equation. When $E_{\rm add}$ is much larger than kT, it is sufficient to take the nth and $(n-1)$th electrons into account. Thus, the general master equation for the probability $P_n(t)$ of capturing the nth SE in the island is

$$\frac{dP_n(t)}{dt} = -\Gamma_n^{\rm out}(t)P_n(t) + \Gamma_n^{\rm in}(t)[1 - P_n(t)], \qquad (4)$$

where $\Gamma_n^{\rm in}(t)$ is the rate at which the nth SE enters the island from the lead. When we assume parabolic potential barriers with a much larger barrier height than kT under a lower gate, $\Gamma_n^{\rm out}(t) = \Gamma_{n0}\exp[-\beta(t - t_0)]$ and $\Gamma_n^{\rm in}(t) = \Gamma_n^{\rm out}(t)\exp(\frac{-U_{\rm IS}}{kT})$, where Γ_{n0} and β are time-independent constants (β is detailed later) and $U_{\rm IS}$ is the electron potential in the island and is aligned with the Fermi level in the lead at $t = t_0$. With linear ramping of the pulse voltage $-\Delta V_{\rm LG}t/t_{\rm rise}$ applied to LG1 or LG2, $U_{\rm IS} = e\alpha_{\rm I}\Delta V_{\rm LG}(t - t_0)/t_{\rm rise}$, where $\Delta V_{\rm LG}$ is the amplitude of the pulse voltage, and $\alpha_I = C_{\rm C}/C_\Sigma$. $\Gamma_n^{\rm out}(t)$ can be divided into two terms: thermal hopping ($\beta = \beta^{\rm h}$) and tunneling ($\beta = \beta^{\rm t}$). We define the transition temperature T_0 from the thermal hopping to the tunneling; T_0 ($= \hbar\omega/2k\pi$) is determined by the curvature of the parabolic potential barrier $U(x) = U - m^*\omega^2x^2/2$, where $\hbar$ is Planck's constant, U is the potential barrier hight, and m^* is the effective mass of an electron in Si [26]. In both thermal hopping and tunneling, β is related to the potential barrier height with respect to the island electron potential [see also Fig. 5(b)]: $U - U_{\rm IS} = e(\alpha_{\rm LG} - \alpha_{\rm I})\Delta V_{\rm LG}(t - t_0)/t_{\rm rise} + {\rm const.}$, where $e\alpha_{\rm LG}$ is a conversion factor from $V_{\rm LG}$ to the corresponding energy. When $C_{\rm C} = 0$, $\Gamma_n^{\rm in}(t)/\Gamma_n^{\rm out}(t)$ is independent of time and Eq. (4) is solved exactly on condition that the system initially follows the thermal equilibrium. This simply results in the final ($t \to \infty$) probability distribution also reaching thermal equilibrium. With finite $C_{\rm C}$, $\Gamma_n^{\rm in}(t)/\Gamma_n^{\rm out}(t)$ depends on time. As time increases, $\Gamma_n^{\rm in}(t)$ becomes smaller than $\Gamma_n^{\rm out}(t)$. When $\Gamma_n^{\rm in}(t) \ll \Gamma_n^{\rm out}(t)$, the second term on the right-hand side of Eq. (4) is neglected, corresponding to the pure decay cascade model. We define the boundary as $\Gamma_n^{\rm in}(t_{\rm a})/\Gamma_n^{\rm out}(t_{\rm a}) = e^{-1}$. This condition yields the characteristic time $t_{\rm a} - t_0 = kTt_{\rm rise}/e\alpha_{\rm I}\Delta V_{\rm LG}$. When the decay cascade model is applied soon after $t = t_0$ (i.e., $t_{\rm a} - t_0$ is very small), the solution of the master equation is

$$P_n(t) = \exp\left(-\frac{\Gamma_{n0}}{\beta}[1 - \exp\{-\beta(t - t_0)\}]\right). \qquad (5)$$

From this equation, the characteristic time $t_{\rm b}$ for capturing the nth SE can be defined as $t_{\rm b} - t_0 = 1/\beta$. This must be valid because $P_n(t_{\rm b}) \sim [P_n(\infty)]^{0.63}$; the system approaches the final state at $t = t_{\rm b}$. This situation is depicted schematically in Fig. 5(c).

In high-temperature regimes ($T \gg T_0$), $\Gamma_n^{\rm out}(t)$ can be expressed by the thermal hopping model, where $t_{\rm b} - t_0 \sim 1/\beta^{\rm h} \sim kTt_{\rm rise}/e(\alpha_{\rm LG} - \alpha_{\rm I})\Delta V_{\rm LG}$. When Eq. (5) is valid, $t_{\rm a} \ll t_{\rm b}$ because $t_{\rm a} - t_0$ is sufficiently small, yielding $g \equiv \alpha_{\rm I}/(\alpha_{\rm LG} - \alpha_{\rm I}) \gg 1$. This indicates that the mechanism of the SE transfer approaches the decay cascade model when $\alpha_{\rm I}$ ($<\alpha_{\rm LG}$) is sufficiently large, which is achieved by increasing $C_{\rm C}$. Note that g is a similar function to the plunger-to-barrier ratio in Ref. [27]. The opposite limit, $g \ll 1$, can be achieved when $C_{\rm C}$ approaches 0. Since the thermal equilibrium model is valid when $C_{\rm C} = 0$, as discussed above, the mechanism of the SE transfer approaches thermal equilibrium when $g \ll 1$. Thus, the comparison between $t_{\rm a}$ and $t_{\rm b}$ can be used to distinguish the thermal equilibrium model and the decay cascade model.

Then, we consider the low-temperature regimes ($T \ll T_0$), where $\Gamma_n^{\rm out}(t)$ can be expressed by the tunneling model, where $t_{\rm b} - t_0 \sim 1/\beta^{\rm t} \sim kT_0 t_{\rm rise}/e(\alpha_{\rm LG} - \alpha_{\rm I})\Delta V_{\rm LG}$. The decay cascade model and the thermal equilibrium model are valid when $t_{\rm a} \ll t_{\rm b}$ and $t_{\rm a} \gg t_{\rm b}$, respectively, corresponding to $T \ll gT_0$ for the decay cascade model and $T \gg gT_0$ for the thermal equilibrium model. Note that gT_0 is only valid as the crossover point at $T \ll T_0$. The above discussion is summarized in the diagram in Fig. 5(d).

To verify the above qualitative discussion, we numerically calculated the master equation and plotted $P_n(t_{\rm rise})$ as a function of $V_{\rm UG}$ [Fig. 5(e)] (see Appendix A for further information about the model). Then we estimated the ratio R of the two peak heights A^+ and A^- in the second derivative of P_n as shown in Fig. 5(e) ($R = |A^+/A^-|$). Since R is constant for the thermal equilibrium model ($R = 1$: the symmetric rise shape of the current plateaus) and the decay cascade model ($R \sim 1.92$: the asymmetric rise shape of the current plateaus), R is a useful parameter for exploring which mechanism dominates the SE transfer. The circles and triangles in Fig. 5(f) show estimated R as a function of temperature, where g is 0.25 and 9, respectively, and T_0 is 20 K. When g is large, corresponding to a large $C_{\rm C}$, R has a slight dependence on temperature and is close to the value in the decay cascade model. On the other hand, when g is small, corresponding to a small $C_{\rm C}$, R is close to the value in the thermal equilibrium model at high temperature and approaches the value in the decay cascade model below $T \sim gT_0$. These results are consistent with the above qualitative discussion.

E. Experimental observation of mechanism crossover and prospects for high-accuracy SE transfer

Figure 6(a) shows a magnified plot of the $2ef$ plateau for an SE ejection (red dots), in which the voltage conditions are the same as those in the shuttle error measurements [28]. Data with a wide $V_{\rm UG}$ range are shown in the inset. We fit the plateau by using the thermal equilibrium and decay cascade models. Despite the low base temperature, the fit obtained by using the former agrees better with the experimental data than that obtained with the latter, which is validated by comparing the reduced χ^2 values of the fit [R-χ^2 in Fig. 6(a)]. From the fit obtained with the thermal equilibrium model, we extracted $E_{\rm add}/kT$, which determines the error rate. Then, we estimated the theoretical lower bound of the error rate, $P_{\rm error}^{\rm thermal} = e^{-E_{\rm add}/2kT}/(1/2 + e^{-E_{\rm add}/2kT})$, which was about 24 ppm. This error rate corresponds to that at the center of the $2ef$ plateau. The order of the error rate extracted from the fit is similar to that of the experimental value (about 100 ppm), indicating that thermal fluctuation may limit the error rate in the shuttle error measurements. The small difference in the error between the fit and the experiment could be due to the charging effect in the node; the operating point may not be located at the point with the theoretically minimum error rate. Note that the current fluctuation in Fig. 6(a) (measurement uncertainty $\sim 10^{-2}$) is not related to the error of the 2-SE transfer but to the measurement noise because the actual error rate at this voltage is around 100 ppm, which is determined by the shuttle error measurement.

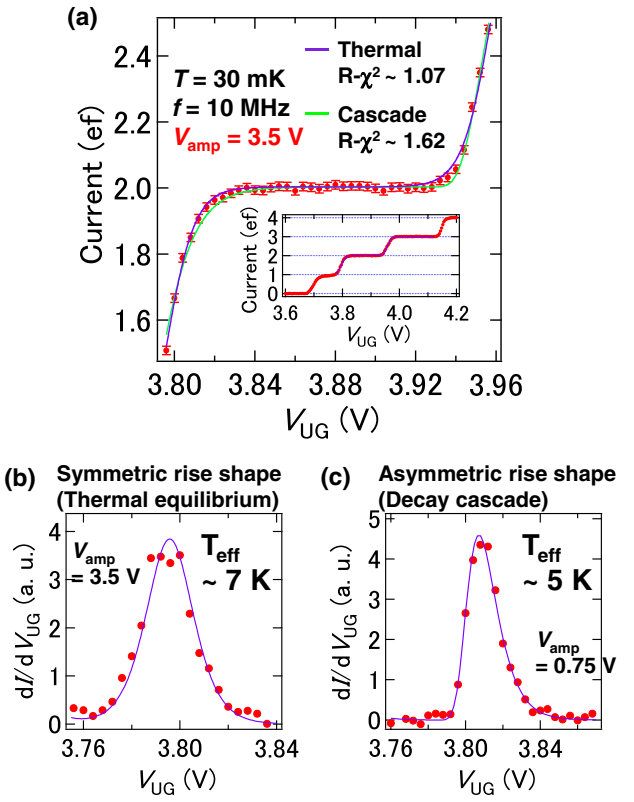

FIG. 6. (Color online) (a) Current, which is normalized by ef, passing through the SE transfer device (red dots) as a function of $V_{\rm UG}$ ($V_{\rm LG3} = 1.5$ V, $V_{\rm S} = 0.5$ V, $V_{\rm D} = 0.9$ V). $V_{\rm LG1}$ and $V_{\rm LG2}$ are modulated between -3 and 0.5 V. $V_{\rm amp}$ is the amplitude of the pulse voltage. The purple and green curves are theoretical fits obtained with the thermal equilibrium model and the decay cascade model, respectively. The range of the fit is between $\sim 1.5ef$ and $\sim 2.5ef$. R-χ^2 is the reduced χ^2 value of the fit. (Inset) Current normalized by ef as a function of $V_{\rm UG}$, where the $2ef$ plateau corresponds to that in the main panel. The blue curve is the fit obtained with the thermal equilibrium model. (b),(c) The first derivative of the SE-transfer current as a function of $V_{\rm UG}$ with the fit obtained with the thermal equilibrium (b) and decay cascade (c) models, where $V_{\rm amp} = 3.5$ and 0.75 V in (b) and (c), respectively. The remaining voltage conditions are the same as those in (a).

To investigate the influence of the thermal fluctuations, we changed the base temperature to 1 K, but the plateau shape did not change, indicating that there is another heat source. Then, we reduced the amplitude of the pulse voltage applied to LG2 ($V_{\rm amp}$) at the base temperature. As $V_{\rm amp}$ was reduced from 3.5 to 0.75 V, the symmetric rise shape of the plateaus became asymmetric as shown Figs. 6(b) and 6(c), indicating that the SE-transfer mechanism changed from the thermal equilibrium model to the decay cascade model [29]. Thus, we speculate that heating is induced by the pulse power. Note that similar heating has been reported in an Si SE transfer device [30]. To estimate the effective temperature $T_{\rm eff}$ in the thermal equilibrium model, we used the electron addition energy estimated from a device with the same geometry [18] ($\sim$14 meV) and obtained $T_{\rm eff} \sim 7$ and 5 K at $V_{\rm amp} = 3.5$ and 0.75 V, respectively. Note that this is a crude estimation at $V_{\rm amp} = 0.75$ V because the SE transfer is explained well with the decay cascade model. Since these

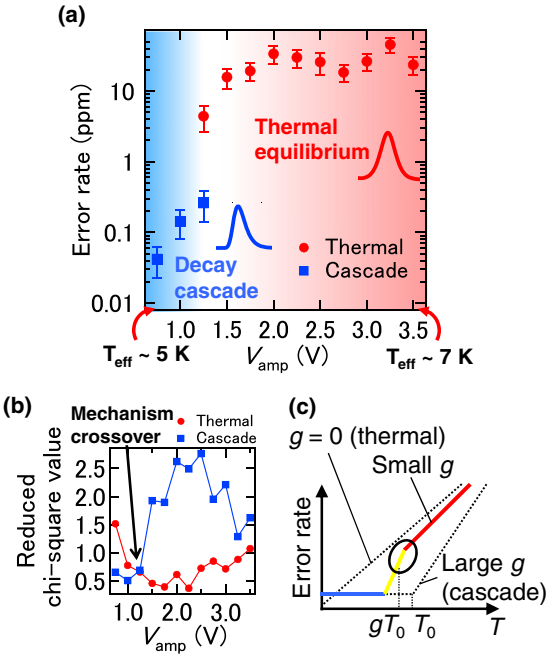

FIG. 7. (Color online) (a) Error rates estimated from $E_{\rm add}/kT$ or δ_3, which are extracted from the fits to the 2ef plateau with the thermal equilibrium (red dots) or decay cascade (blue squares) models, respectively, as a function of $V_{\rm amp}$. The error bars are calculated from the standard deviations of $E_{\rm add}/kT$ and δ_3 extracted from the fits. (b) The reduced χ^2 values obtained by the fits performed in (a) as a function of $V_{\rm amp}$, where the circles and squares correspond to the thermal equilibrium and decay cascade models, respectively. (c) Theoretically expected error rate for three different conditions of g as a function of temperature (the scale of the vertical axis is logarithmic).

temperatures are much higher than the base temperature, a further decrease in $T_{\rm eff}$ might be possible by optimizing $V_{\rm amp}$.

We then estimated the theoretical lower bound of the error rate from $E_{\rm add}/kT$ or $\delta_3 \equiv \Delta_3 - \Delta_2$, which was extracted from the fit to the $2ef$ plateau by the thermal equilibrium or decay cascade models, respectively. Note that the error rate at the $2ef$ plateau for the decay cascade model is determined by δ_3 and we define the theoretical lower bound of the error rate for the decay cascade model as the error rate at the point of inflection in the fitting curve [16] (details are discussed in Appendix B). For a proper comparison, the range of the fit was fixed at between $\sim 1.5ef$ and $\sim 2.5ef$, which is the same as that in Fig. 6(a). Figure 7(a) shows the error rate as a function of $V_{\rm amp}$. When plotting these results, we compared the reduced χ^2 values of the two fits by the two models at the same $V_{\rm amp}$ [Fig. 7(b)] and selected the result with the smaller reduced χ^2 value. At $V_{\rm amp} = 1.25$ V, the reduced χ^2 values cross over [see the arrow in Fig. 7(b)]. This indicates that the actual error rate should be close to the value extracted by the decay cascade model at a low $V_{\rm amp}$.

Figure 7(c) shows the theoretically expected error rate as a function of temperature. When $g = 0$ (thermal equilibrium), the error rate decreases exponentially with decreasing temperature. The opposite limit is sufficiently large g (decay cascade), where the error rate decreases exponentially at $T > T_0$ and saturates at $T < T_0$ with decreasing temperature. This saturation is due to the temperature-independent tunneling rate. Note that the decay cascade model yields lower error rates than the thermal equilibrium model at $T > T_0$ because of the asymmetric probability of the SE capture into the island as a function of $V_{\rm UG}$ [see Eq. (3)]. When g is small, the temperature dependence of the error rate is similar to that in the thermal equilibrium model at $T \gg gT_0$ (red line), the mechanism changes at $T \sim gT_0$ (yellow line), and the error rate saturates at $T \ll gT_0$ (blue line). Since the reduced χ^2 values cross over in Fig. 7(b), the region indicated by the black circle in Fig. 7(c) may correspond to the temperature regime in Fig. 7(a).

The lowest estimated error rate is about 0.04 ppm at $V_{\rm amp} = 0.75$, demonstrating the potential of the Si SE transfer device for metrological applications [31]. Moreover, it should be possible to further reduce the theoretical lower bound of the error rate by optimizing the voltage condition because we did not observe the error saturation. As a next step, we will investigate the error saturation to know maximum performance of the device. In addition, the error rate may increase at a higher frequency due to negligible effects at the low frequency. The most important effect would be the nonadiabatic excitation effect, by which the SE captured in the island escapes to the lead through the excited state [17]. Thus, the error estimation at a higher frequency is the most important future work.

Finally, we suggest ways to achieve SE transfer with higher accuracy. Since $\delta_{\rm n+1} = E_{\rm add}/kT_0$ at $T \ll T_0$ determines the error rate, $E_{\rm add}$ and T_0 should be large and small, respectively. The former can be achieved by scaling down the island size. Since $T_0 = \hbar\omega/2k\pi$, the slope of the potential barrier should be gentle to reduce T_0. This indicates that the gate should be sufficiently long, although the influence of the trap level and the surface roughness may increase. Alternatively, by using one more pulse voltage that fixes the island potential (effectively $\alpha_{\rm I} \to 0$), the thermal equilibrium model can hold at low temperature and the saturation of the error rate by the decay cascade model with the tunneling can be ignored. This could yield a much lower error rate than that in the above estimation with decreasing temperature.

IV. CONCLUSION

We used single-shot shuttle error measurements to estimate an error rate of about 100 ppm in Si SE turnstiles at a base temperature of 30 mK. The charging effect in the node influences the error rate in this measurement; the error rate of the 2-SE ejection was estimated while $N_{\rm node}$ remained the same during each cycle of the 2-SE shuttle transfer. In addition, a heating effect caused by the pulse voltage may degrade the error rate because the current plateau, which has the same voltage condition as that in the shuttle error measurements, is fitted well by the thermal equilibrium model and the extracted error rate is in reasonable agreement with the experiment. Moreover, as the pulse voltage amplitude decreases, the transfer mechanism changes from the thermal equilibrium model to the decay cascade model. We discussed the crossover point of the transfer mechanism; it is the transition temperature T_0 or gT_0, which mainly depends on the capacitive coupling between a lower gate and the island and on the potential barrier shape. The lower bound of the

error rate estimated by the theoretical fit is about 0.04 ppm at the minimum pulse amplitude and it should be further reduced by optimizing the voltage condition, which implies that the Si SE transfer device has the potential to satisfy the criteria for quantum current standards.

ACKNOWLEDGMENT

This work was partly supported by the Funding Program for Next Generation World-Leading Researchers of JSPS (GR 103).

APPENDIX A: MODEL OF NUMERICAL CALCULATION

We assume that the island has a single energy level for the nth electron and the shape of the electrostatically induced barrier (the height is much higher than kT) is parabolic. For simplicity, we assume a single energy level for the thermal hopping. We need to explicitly express the effect of the change in $U_{\rm IS}$ caused by $V_{\rm UG}$, which is included in t_0 in the main text. Then, $\Gamma_n^{\rm out}(t)$ and $\Gamma_n^{\rm in}(t)$ are modeled as

$$\Gamma_n^{\rm out}(t) = \Gamma_{n0}^{\rm h}\exp\left(-\beta^{\rm h}t - \frac{e\alpha_{\rm UG}V_{\rm UG}}{kT}\right) + \Gamma_{n0}^{\rm t}\exp\left(-\beta^{\rm t}t - \frac{e\alpha_{\rm UG}V_{\rm UG}}{kT_0}\right)(1-f), \quad \text{(A1)}$$

$$\Gamma_n^{\rm in}(t) = \Gamma_n^{\rm out}(t)\exp\left(-\frac{e\alpha_{\rm I}\Delta V_{\rm LG}t/t_{\rm rise} - e\alpha_{\rm UG}V_{\rm UG}}{kT}\right), \quad \text{(A2)}$$

$$f = \left[1+\exp\left(\frac{e\alpha_{\rm I}\Delta V_{\rm LG}t/t_{\rm rise} - e\alpha_{\rm UG}V_{\rm UG}}{kT}\right)\right]^{-1}, \quad \text{(A3)}$$

where $\alpha_{\rm UG} = C_{\rm UG}/C_\Sigma$ and f is the Fermi-Dirac distribution of the lead. $\Gamma_{n0}^{\rm h}$ and $\Gamma_{n0}^{\rm t}$ are the initial escape rates for the thermal hopping mechanism and the tunneling mechanism, respectively; in the initial state ($t = 0$, $V_{\rm UG} = 0$), the electrochemical potential in the island is aligned with the Fermi level in the lead and $\Gamma_{n0}^{\rm t}$ and $\Gamma_{n0}^{\rm h}$ can be expressed using the initial potential barrier hight $\Delta_{\rm i}$ and constant Γ_0 as $\Gamma_{n0}^{\rm t} = \Gamma_0\exp(-\Delta_{\rm i}/kT_0)$ and $\Gamma_{n0}^{\rm h} = \Gamma_0\exp(-\Delta_{\rm i}/kT)$. In addition, we assume that the occupation probability in the lead is 0 for the hopping mechanism ($f \sim 0$) because the potential barrier height should be sufficiently large in the range of parameters discussed below.

To observe the change in R at $T \sim T_0$ and gT_0, we set $T_0 \sim 20$ K (a typical value in MOSFETs) and $g = 0.25$ (weak coupling) or $g = 9$ (strong coupling). From a measured subthreshold slope S in a MOSFET similar to that comprised of a lower gate ($S \sim 100$ mV/decade at $T = 100$ K), we extract $\alpha_{\rm LG} = \ln 10 \times kT/eS \sim 0.2$. Note that $g = 0.25$ and 9 correspond to $\alpha_{\rm I} = 0.04$ and 0.18, respectively. We assume that $\Gamma_{n0}^{\rm t}$ can be estimated by the quantized resistance $R_{\rm Q} \sim 26\ {\rm k}\Omega$ and the island capacitance $C_\Sigma \sim 11$ aF (corresponding to $E_{\rm add} \sim 14$ meV [18]) as $\Gamma_{n0}^{\rm t} = 1/2\pi R_{\rm Q}C_\Sigma \sim 5\times10^{11}$. Although it is difficult to ascertain $\Delta_{\rm i}$ exactly, we roughly estimate it as follows. Since an energy of $T_0 = 20$ K corresponds to about 2 meV and the maximum barrier height at which we could measure the current in the subthreshold region is about 20 meV, $\Delta_{\rm i}$ should fall between these two values. Thus, we use $\Delta_{\rm i} = 10$ meV, corresponding to a barrier width d of about 7 nm estimated by the parabolic potential model $\Delta_{\rm i} - m^*\omega^2d^2/2$ and $T_0 = \hbar\omega/2k\pi = 20$ K. Since the gate length L of the lower gate is about 30 nm, the order of the barrier width is reasonable ($L > d$). Then we obtain $\Gamma_{n0}^{\rm h} = \Gamma_{n0}^{\rm t}\exp(\Delta_{\rm i}/kT_0)\exp(-\Delta_{\rm i}/kT)$. Furthermore, we set $\Delta V_{\rm LG} = 0.75$ V, $t_{\rm rise} = 2$ ns, and $\alpha_{\rm UG} = 0.1$. Note that the correspondence between the parameters in the appendix and those in the main text is as follows: $t_0 = \alpha_{\rm UG}V_{\rm UG}t_{\rm rise}/\alpha_{\rm I}\Delta V_{\rm LG}$ and $\Gamma_{n0} = \Gamma_0\exp[-(\Delta_{\rm i} + e\alpha_{\rm LG}\Delta V_{\rm LG}t_0/t_{\rm rise})/kT]$.

APPENDIX B: ERROR RATE FOR DECAY CASCADE MODEL

The error rate $P_{\rm error}^{\rm cas}(V_{\rm UG})$ at the $2ef$ plateau for the decay cascade model is given by [25]

$$P_{\rm error}^{\rm cas}(V_{\rm UG}) = 1 - P_2(V_{\rm UG}) \quad \text{(B1)}$$

$$= 1 - \exp[-\exp(-\alpha_{\rm UG}V_{\rm UG} + \Delta_2)] + \exp[-\exp(-\alpha_{\rm UG}V_{\rm UG} + \Delta_3)], \quad \text{(B2)}$$

where $P_2(V_{\rm UG})$ is the capture probability of two SEs. Since the plateau is flattest at the point of the inflection ($V_{\rm Inf}$), we define the theoretical lower bound of the error rate as the error rate at $V_{\rm UG} = V_{\rm Inf}$. We extracted $V_{\rm Inf}$ from the derivative of the fitting curve. By using constant $\gamma_{\rm Inf}$, $V_{\rm Inf}$ is determined as $V_{\rm Inf} = \Delta_2/\alpha_{\rm UG} + \gamma_{\rm Inf}(\Delta_3/\alpha_{\rm UG} - \Delta_2/\alpha_{\rm UG})$, where $\Delta_2/\alpha_{\rm UG}$ and $\Delta_3/\alpha_{\rm UG}$ are the respective positions at which the $2ef$ and $3ef$ plateaus rise. As a result, we find

$$P_{\rm error}^{\rm cas}(V_{\rm Inf}) = 1 - \exp[-\exp(-\delta_3\gamma_{\rm Inf})] + \exp\{-\exp[\delta_3(1-\gamma_{\rm Inf})]\}, \quad \text{(B3)}$$

where $\delta_3 \equiv \Delta_3 - \Delta_2$. Once δ_3 is extracted from the fit to the $2ef$ plateau, the error rate at the point of inflection is estimated from Eq. (B3).

[1] K. Nishiguchi, A. Fujiwara, Y. Ono, H. Inokawa, and Y. Takahashi, Appl. Phys. Lett. **88**, 183101 (2006).

[2] G. Fève, A. Mahé, J.-M. Berroir, T. Kontos, B. Plaçais, D. C. Glattli, A. Cavanna, B. Etienne, and Y. Jin, Science **316**, 1169 (2007).

[3] I. M. Mills, P. J. Mohr, T. J. Quinn, B. N. Taylor, and E. R. Williams, Metrologia **43**, 227 (2006).

[4] M. W. Keller, Metrologia **45**, 102 (2008).

[5] N. Feltin and F. Piquemal, Eur. Phys. J. Spec. Top. **172**, 267 (2009).

[6] H. Pothier, P. Lafarge, C. Urbina, D. Esteve, and M. H. Devoret, Europhys. Lett. **17**, 249 (1992).

[7] L. J. Geerligs, V. F. Anderegg, P. A. M. Holweg, J. E. Mooij, H. Pothier, D. Esteve, C. Urbina, and M. H. Devoret, Phys. Rev. Lett. **64**, 2691 (1990).

[8] M. W. Keller, J. M. Martinis, N. M. Zimmerman, and A. H. Steinbach, Appl. Phys. Lett. **69**, 1804 (1996).

[9] J. P. Pekola, J. J. Vartiainen, M. Möttönen, O.-P. Saira, M. Meschke, and D. V. Averin, Nat. Phys. **4**, 120 (2008).

[10] L. P. Kouwenhoven, A. T. Johnson, N. C. van der Vaart, C. J. P. M. Harmans, and C. T. Foxon, Phys. Rev. Lett. **67**, 1626 (1991).
[11] A. Fujiwara, N. M. Zimmerman, Y. Ono, and Y. Takahashi, Appl. Phys. Lett. **84**, 1323 (2004).
[12] M. D. Blumenthal, B. Kaestner, L. Li, S. Giblin, T. J. B. M. Janssen, M. Pepper, D. Anderson, G. Jones, and D. A. Ritchie, Nat. Phys. **3**, 343 (2007).
[13] A. Fujiwara, K. Nishiguchi, and Y. Ono, Appl. Phys. Lett. **92**, 042102 (2008).
[14] S. P. Giblin, S. J. Wright, J. D. Fletcher, M. Kataoka, M. Pepper, T. J. B. M. Janssen, D. A. Ritchie, C. A. Nicoll, D. Anderson, and G. A. C. Jones, New J. Phys. **12**, 073013 (2010).
[15] M. W. Keller, Eur. Phys. J. Spec. Top. **172**, 297 (2009).
[16] S. P. Giblin, M. Kataoka, J. D. Fletcher, P. See, T. J. B. M. Janssen, J. P. Griffiths, G. A. C. Jones, I. Farrer, and D. A. Ritchie, Nat. Commun. **3**, 930 (2012).
[17] J. D. Fletcher, M. Kataoka, S. P. Giblin, S. Park, H.-S. Sim, P. See, D. A. Ritchie, J. P. Griffiths, G. A. C. Jones, H. E. Beere, and T. J. B. M. Janssen, Phys. Rev. B **86**, 155311 (2012).
[18] G. Yamahata, K. Nishiguchi, and A. Fujiwara, Appl. Phys. Lett. **98**, 222104 (2011).
[19] K. Nishiguchi, C. Koechlin, Y. Ono, A. Fujiwara, H. Inokawa, and H. Yamaguchi, Jpn. J. Appl. Phys. **47**, 8305 (2008).
[20] We verified that the second electron at the $2ef$ plateau was transferred not through the trap level in the barrier but through the island by checking the dependence of the transfer current on the pulse voltage; the capacitive coupling between the island and LG1 at the $2ef$ plateau was almost the same as that at the other plateaus and the threshold voltages of the plateaus were almost independent of the pulse voltage (these features are different for SE transfer through the trap level, which will be published elsewhere).
[21] When the number of transferred electrons is different, the width of the current plateaus along with the V_{UG} axis is also different even in an SE transfer via a charge island [for example, see the $2ef$, $3ef$, and $4ef$ plateaus in Fig. 2(a)]. Such an irregular addition spectrum is often observed in the few-electron regime for semiconductor charge islands, while the spectrum is periodic for metallic islands. One reason for this is the "shell structure" [22] that results from the quantum confinement and electron-electron interaction in the island. Another reason is the effect of the potential fluctuation caused by the width fluctuation of the Si nanowire. In spite of these modifications to the addition spectrum, the width of the current plateaus simply reflects the electron addition energy.
[22] L. P. Kouwenhoven, D. G. Austing, and S. Tarucha, Rep. Prog. Phys. **64**, 701 (2001).
[23] L. Fricke, F. Hohls, N. Ubbelohde, B. Kaestner, V. Kashcheyevs, C. Leicht, P. Mirovsky, K. Pierz, H. W. Schumacher, and R. J. Haug, Phys. Rev. B **83**, 193306 (2011).
[24] P. Lafarge, H. Pothier, E. R. Williams, D. Esteve, C. Urbina, and M. H. Devoret, Z. Phys. B: Condens. Matter **85**, 327 (1991).
[25] V. Kashcheyevs and B. Kaestner, Phys. Rev. Lett. **104**, 186805 (2010).
[26] L. D. Landau and E. M. Lifshitz, *Quantum Mechanics* (Butterworth-Heinemann, Amsterdam, 1981), Vol. 3.
[27] V. Kashcheyevs and J. Timoshenko, Phys. Rev. Lett. **109**, 216801 (2012).
[28] The standard deviation of the data is extracted from the measurement noise; we use a typical value (20 fA) throughout the analysis of the plateau fit in this paper.
[29] This also indicates that the SEs are transferred through the island because we have observed a different rise shape for SE transfer through a trap level (in preparation).
[30] K. W. Chan, M. Möttönen, A. Kemppinen, N. S. Lai, K. Y. Tan, W. H. Lim, and A. S. Dzurak, Appl. Phys. Lett. **98**, 212103 (2011).
[31] It was difficult to perform the shuttle error measurements at a low voltage amplitude because the $-2ef$ plateau is further disturbed, resulting in too many errors in the 2-SE injection. Although we have another device with which there is no trap level induced fluctuation, unfortunately the sensor has insufficient charge sensitivity. In future work, we will optimize the sensor structure and attempt a shuttle error measurement in a device with no fluctuation.